Factors Controlling the Size of Graphene Oxide Sheets Produced *via* the Graphite Oxide Route

Shuyang Pan[†] and Ilhan A. Aksay[†,*]

[†]Department of Chemical and Biological Engineering, Princeton University, Princeton, New Jersey 08544, United States

ABSTRACT We have studied the effect of the oxidation path and the mechanical energy input on the size of graphene oxide sheets derived from graphite oxide. The cross-planar oxidation of graphite from the (0002) plane results in periodic cracking of the uppermost graphene oxide layer, limiting its lateral dimension to less than 30 μm. We use an energy balance between the elastic strain energy associated with the undulation of graphene oxide sheets at the hydroxyl and epoxy sites, the crack formation energy, and the interaction energy between graphene layers to determine the cell size of the cracks. As the effective crack propagation rate in the cross-planar direction is an order of magnitude smaller than the edge-to-center oxidation rate, graphene oxide single sheets larger than those defined by the periodic cracking cell size are produced depending on the aspect ratio of the graphite particles. We also demonstrate that external energy input from hydrodynamic drag created by fluid motion or sonication, further reduces the size of the graphene oxide sheets through tensile stress buildup in the sheets.

KEYWORDS: graphene oxide · periodic cracking · size reduction

Interest in graphene stems from its exceptional mechanical properties (Young's modulus of 1 TPa, tensile strength of 130 GPa),[1] electron mobility (2×10^5 cm^2/(V s)),[2] and high surface area (1850−2630 m^2/g).[3] These properties make graphene a promising material for multifunctional composites, high performance electrodes for energy storage, and catalysis applications.[4−14]

While graphene sheets have been produced in small quantities through chemical vapor deposition,[15−17] epitaxial growth,[18] and mechanical peeling with a scotch tape,[19] industrial scale manufacturing has only been possible with the use of graphite oxide (GO), which is obtained through oxidation of graphite.[20,21] GO is then split apart into individual sheets either through rapid heating[3,22] or ultrasonication[10] to yield functionalized graphene sheets (FGSs) with varying carbon-to-oxygen atomic ratios, C/O. The lateral size of functionalized graphene sheets produced by the GO splitting has a significant impact on the properties of graphene-based electrodes and composites.[23−25] The electrical conductivity of graphene aggregates is dominated by the contact resistance between the graphene sheets.[26] Larger graphene sheets can reduce the number of graphene−graphene contacts for a given number of conducting paths and hence reduce the total contribution of contact resistance and enhance the conductivity.[23] Larger sheets can be more effective in load transfer when graphene is used as a reinforcement filler in composites.[24] Furthermore, plate-like fillers can reduce gas permeability of polymeric matrices by increasing the diffusion path length of gas molecules.[25] The magnitude of the reduction is proportional to the aspect ratio of fillers, and larger graphene sheets are expected to be more effective at reducing gas permeabilities.

Previous studies have addressed the size limitation of graphene oxide sheets to some extent.[3,27−29] McAllister *et al.*[3] showed that the lateral size of GO obtained by completely oxidizing (as defined by the elimination of the graphite peak in the X-ray diffraction (XRD) pattern) all graphite particles (using the Staudenmaier method[21]) was limited to tens of micrometers regardless of the size of the starting graphite particle, indicating that the controlling factor is not the size of graphite particles. However, recently, Zhao *et al.*[27] showed that the C/O of the GO derived from Hummers oxidation[20] had a significant effect on the size of graphene oxide sheets. While large-area graphene oxide sheets (*e.g.*, up to 220 μm, the lateral size is obtained from our analysis of the scanning electron microscopy (SEM) images of graphene oxide in ref 27) were obtained by sonicating GO with a C/O at 2.63 for 5 min, the lateral size of the sheets was mostly reduced to less than 10 μm when the C/O of GO decreased to 2.08. Recognizing that the formation of epoxy groups on graphene upon oxidation could weaken the sheets,[30] the authors attributed the size reduction of the sheets with increased oxygen content to the higher density of carbon−oxygen bonds, allowing cracks to

* Address correspondence to iaksay@princeton.edu.

Received for review February 17, 2011 and accepted April 6, 2011.

Published online ■■■
10.1021/nn200666r

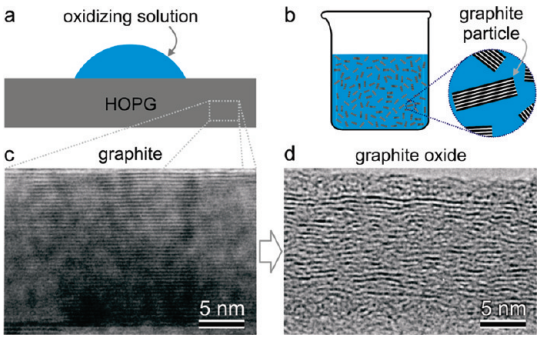

Figure 1. (a) Cross-planar oxidation of an HOPG surface by placing a sessile drop of the oxidizing solution on the upper surface. (b) Oxidation of graphite particles through the edges as well as in cross-planar direction by dispersing them in the oxidizing solution. (c) Cross-sectional transmission electron microscopy (TEM) image of graphite. (d) Cross-sectional TEM image of GO produced by the Staudenmaier method. The TEM images are adapted from ref 3. Copyright 2007 American Chemical Society.

form more easily during sonication. The reduction in graphene oxide size with increasing degree of oxidation was also reported by Zhang *et al*.[28] Su *et al*. applied sonication to graphite particles during the oxidation and showed that the size of graphene oxide sheets obtained decreased with increasing sonication time.[29]

Two fundamental issues remain unclear: (i) In all reported studies so far, the size of graphene oxide sheets has always been smaller than that of the starting graphite.[3,10,22,27,28,31,32] Is it possible to produce graphene oxide sheets with the same lateral size as that of the starting graphite particles? If not, what are the limitations? (ii) At the lower limit, graphene oxide sheets with an average size of 24 nm have been reported.[28] Can the lateral dimension of graphene oxide sheets be reduced to a few nanometers, since at a fully oxidized state, with a C/O of ~2, the epoxy and hydroxyl lines are separated from each other on the order of nanometers?[33] To respond to these questions, in this paper, we provide a detailed study on the parameters that affect the size of functionalized graphene sheets produced by the GO route.

In the first three parts of this study, we address the effect of a cross-planar oxidation path on the size of graphene oxide and GO and establish a crack formation mechanism during the oxidation of graphene sheets. We perform cross-planar oxidation only by deploying a sessile drop of Hummers' oxidizing solution onto a highly ordered pyrolytic graphite (HOPG) surface, as depicted in Figure 1a (in contrast to submerging the graphite particles in the solution, Figure 1b) so that oxidation starts only from the top surface. As the top graphene layer cracks and the solution penetrates into the underneath layers, cells with lateral size of 5−30 μm form. To explain the cracking of graphene sheets and the limiting size of the cells during oxidation, we draw an analogy to the periodic cracking of brittle thin films to relieve stored elastic energy.[34−36] We note that as hydroxyl and epoxy sites form on the graphene sheet during oxidation, the graphene oxide sheets (Figures 1c,d) undulate.[3,30,33,37] But the undulation is constrained due to the attractive interaction between the uppermost graphene sheet and the sheet underneath, thus resulting in an elastic strain energy buildup. The elastic strain energy is released upon cracking and is balanced by the change in interlayer interaction energy and the crack formation energy. This energy balance defines the cell size of the cracked sheets and provides a proof-of-concept support for our experimental results. Crack propagation in the cross-planar direction results in a limiting size for the GO.

Recognizing that in engineering applications, graphite particles will be completely immersed in an oxidizing solution, in the next part of the study, we work with graphite suspensions (Figure 1b) and demonstrate that the size of the GO and thus graphene oxide is controlled not only by a balance of edge-to-center penetration *versus* crack propagation rates but also by the degree of graphite oxidation. We show that the edge-to-center penetration rate is higher than the crack propagation rate. Consequently, when ~700 μm graphite particles are immersed in an oxidizing solution, we obtain GO particles with an average size over 100 μm, which is significantly larger than the expected size of GO obtained from a cross-planar oxidation alone.

In the last part of this study, we address the mechanical energy input on the size of GO particles and graphene oxide sheets derived from GO. Large (*e.g.*, ~100 μm) graphene oxide sheets are only produced from partially oxidized graphite particles when long-duration mechanical shaking (6−12 h) or sonication is avoided. Otherwise, the graphene oxide sheets break down. We propose that cracks in isolated graphene oxide sheets continue to form as sufficient tensile load is transferred to the sheets through the fluid phase of the suspension.

RESULTS AND DISCUSSION

Periodic Cracking of Graphene Sheets during a Cross-Planar Oxidation. The evolution of patterns observed by contact-mode atomic force microscopy (AFM) on HOPG exposed to a sessile drop of the oxidizing solution is summarized in Figure 2. Prior to oxidation, the HOPG surface is featureless at the magnification used (Figures 2a,b). After oxidation for 6 and 60 s, a cellular structure is observed (Figures 2c−f). Statistical analysis reveals a mean cell size of ~16 μm with a similar size distribution on both oxidized surfaces (insets in Figures 2d,f), suggesting that the cell size is not affected by the oxidation time. The edges of the cells are elevated by 17−250 nm with respect to the centers on the surface oxidized for 6 s. The height difference between the centers and edges of the cell increases to 80−300 nm, and the cell edges widen after 60 s of oxidation.

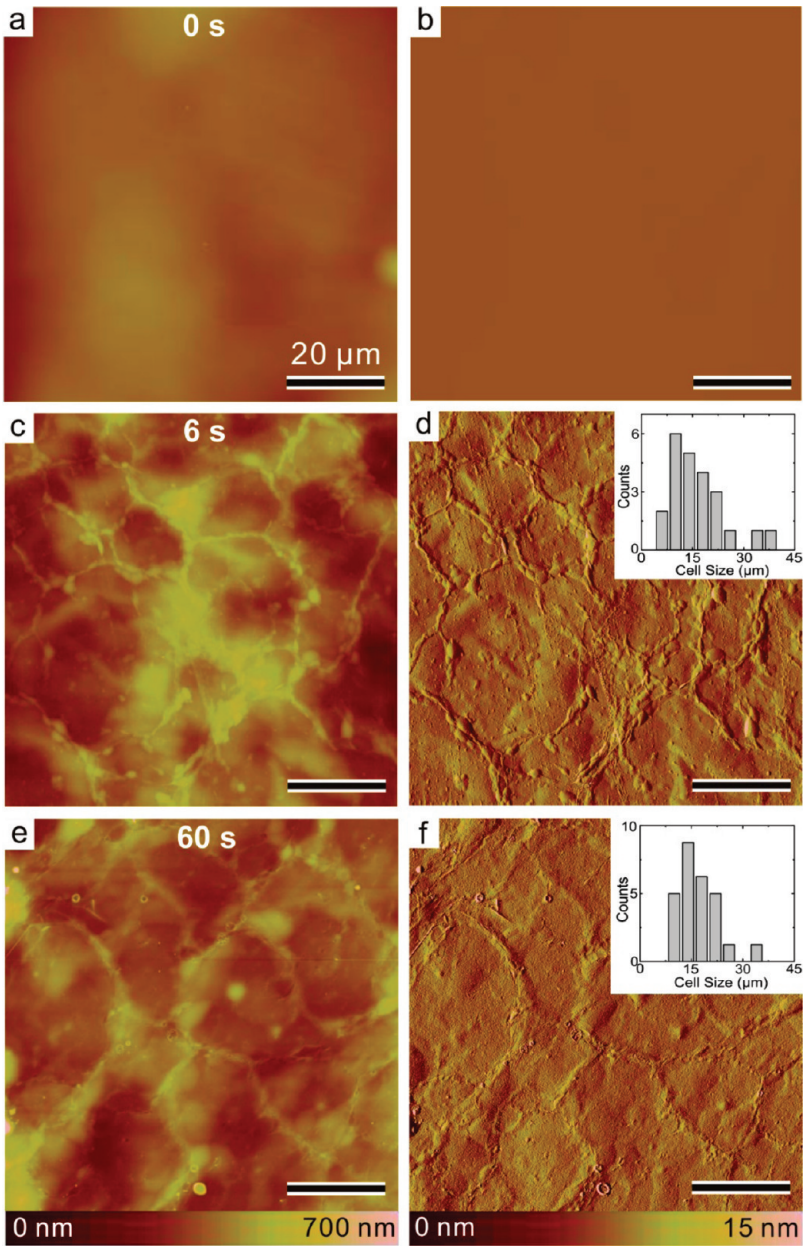

Figure 2. Contact-mode AFM images of HOPG prior to oxidation (a, b) and after being oxidized for 6 s (c, d) and 60 s (e, f). Both height (a, c, e) and deflection images (b, d, f) were recorded. Insets in panels d and f are the histograms of respective cell sizes. The length, height, and deflection scale bars are 20 μm, 700 nm, and 15 nm, respectively.

To further confirm the formation of a cellular structure, the oxidized surfaces were also characterized by optical microscopy and the results are summarized in Figure 3. While the HOPG surface prior to oxidation is again featureless (Figure 3a), after oxidation for 6 s, 60 s, and 10 min (Figures 3b–d), a cellular structure defined by black lines and with interference patterns is observed. The mean cell size is 13–14 μm and the size distribution is similar on all three surfaces (insets in Figure 3b–d), in agreement with the results obtained by AFM. While black lines and interference patterns are present at the edges of the cells on HOPG oxidized for 6 s, in the case of the 60 s and 10 min sample, the cell edges show mostly interference patterns.

To provide a deeper understanding of the cell formation, we examine the colors of the interference patterns located at the cell boundaries on HOPG oxidized for 6 s. While some patterns appear to be blue, others show fringes of different colors, such as red. These observations suggest the presence of an optically transparent, perhaps dielectric layer within the HOPG. The optical thickness *nd* (with *n* being the refractive index and *d* the thickness) of thin dielectric films can be estimated based on the observed interference colors. Once a growing film reaches a thickness corresponding to half the wavelength of the visible range of the electromagnetic spectrum, constructive interference occurs for the matching light wave upon

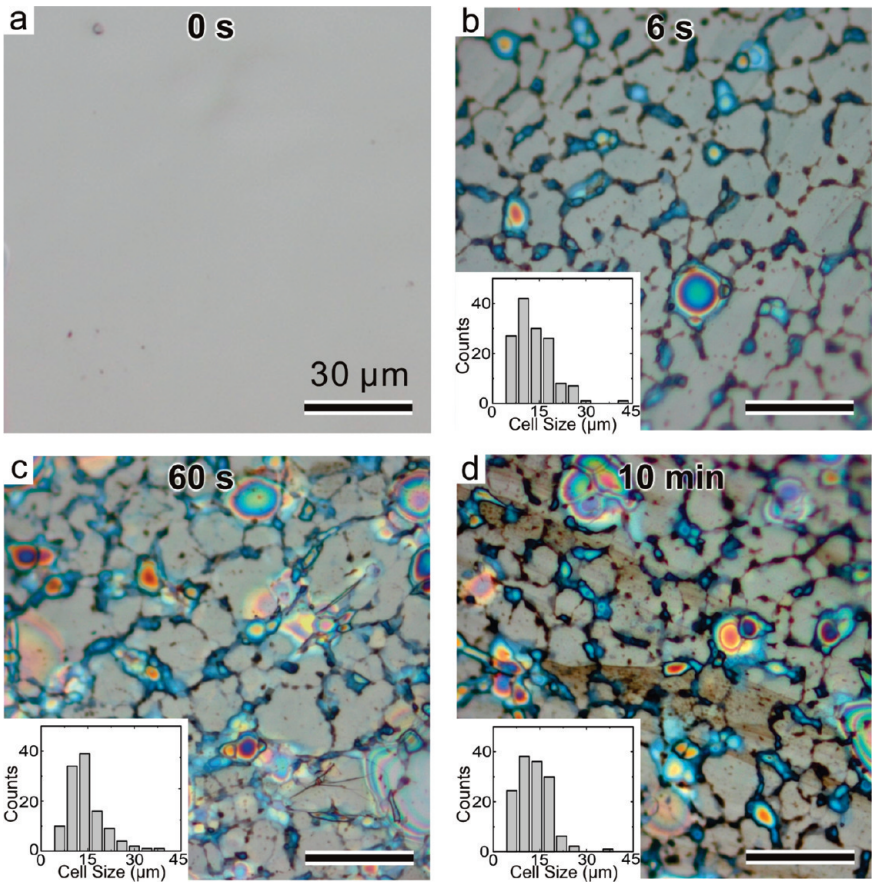

Figure 3. Bright-field optical microscopy images of HOPG prior to oxidation (a) and after being oxidized for 6 s (b), 60 s (c) and 10 min (d). Insets in panels b, c, and d are the histograms of respective cell sizes. All scale bars are 30 μm.

reflection at this layer, and a distinct color can be observed. Depending on illumination and the nature of the substrate, colors from violet over blue, green, and yellow to red can be observed. In case the film thickness increases beyond half the wavelength of red light, a similar color pattern repeats since now diffraction colors can be observed in "second order". Films with inhomogeneous thickness can thus display a complicated pattern of interference fringes, where the color and the number of the fringes indicate the local film thickness.

From this we conclude that the film present on our 6 s HOPG samples showing mostly blue interference color must have a thickness between 100 and 200 nm (for $1< n < 2$, as most materials have refractive indices in this range). In regions where red interference color is observed, the film thickness can be up to 350 nm. The number of fringes within our cell structure increases with oxidation time suggesting a thickening of the surface film up to more than 1 μm.

To explain the origin of the black lines observed in the optical microscopy images, we note that there exists a large variation in the width of cell edges on HOPG oxidized for 6 s, between 2 and 17 μm as shown in the AFM images (Figures 2c,d). The narrow edges have a high surface curvature and thus can scatter light in different directions, resulting in the black color,[38] whereas the wider edges have a lower curvature and are capable of reflecting light, resulting in the interference patterns. With increasing oxidation time, the film grows laterally and such growth reduces the surface curvature, as evidenced by the widening of cell edges in the AFM images (Figures 2e,f), resulting in more interference patterns at the edges of the cells.

As it has been demonstrated that GO has a lower dielectric constant and thus lower refractive index than graphite,[39,40] we attribute the interference patterns to the formation of graphene oxide layers. The appearance of the interference patterns at the cell edges, in conjunction with the elevated cell boundaries as observed by AFM, suggests that the cellular structure is the outcome of periodic cracking in the uppermost graphene layer and the infiltration of the oxidizing solution through the cracks to the underneath layers results in the oxidation of underneath graphene layers and thus elevated boundaries and interference patterns. The 3-fold symmetry of the cracks (Figure 2) is attributed to the honeycomb structure of the graphene lattice.

Four questions are raised based on the observation presented above: (i) Why do the graphene sheets crack during graphene to graphene oxide transition?

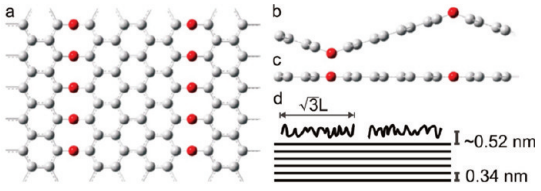

Figure 4. (a) A partially oxidized graphene sheet containing epoxy lines in planar view prior to the tensile deformation; oxygen and carbon atoms are shown in red and gray, respectively. (b) An edge view of panel a; epoxy lines cause the sheet to undulate. (c) The sheet is completely flattened upon the application of tensile strain. (d) Schematic of undulation and crack formation on the uppermost graphene oxide sheet.

(ii) What defines the size of the cells (or graphene oxide sheets) after cracking? (iii) Why does the cell size remain the same with increasing oxidation time? (iv) How do the graphene sheets underneath the top layer crack? We address the first three questions in the next subsection and the last question in the subsection after.

Mechanism of Periodic Cracking. Analogous to the periodic cracking of a brittle thin film deposited on a polymeric substrate subjected to tensile deformations,[34,35] we attribute the periodic cracking of the graphene oxide layers to the buildup of elastic strain energy in the sheets due to the undulation of the sheet as epoxy and hydroxyl sites form.[30,33,37] It has been shown[22] that that epoxy lines cause a graphene oxide sheet to undulate and the application of tensile strain should result in flattening of the sheet as schematically illustrated in Figure 4a–c. We note that carboxylic groups can only form at the edges and vacancy defects of a graphene sheet.[41] As the density of vacancy defects in HOPG is very low,[42] carboxylic sites would not contribute significantly to the buildup of elastic strain energy. The undulation of graphene oxide at hydroxyl and epoxy sites is constrained due to the attractive interaction between the uppermost sheet and the layer underneath it, leading to the buildup of elastic strain energy. When a threshold strain energy is reached, crack formation and undulation of graphene oxide sheet take place. As undulation increases the separation between graphene sheets (Figure 4d), the attractive interaction between the sheet decreases.[3] Therefore, work is done by the graphene oxide sheet to overcome the initial interlayer attraction and increase the interlayer separation. Elastic strain energy is released and further undulation is constrained by the weakened interlayer attraction. Assuming energy dissipation in the form of heat is negligible, the strain energy released is converted to work necessary to increase the interlayer separation and the crack formation energy.

We estimate the cell size based on such an energy balance. Cells are modeled as hexagons with an edge length L, and the cell size is defined as the separation between two parallel edges, $3^{1/2}L$ (Figure 4d). The energy balance is described as

$$E_{\text{crack}} + \Delta E_{\text{interlayer}} = \Delta E_s \quad (1)$$

where E_{crack} is the crack formation energy, $\Delta E_{\text{interlayer}}$ is the work done to increase the interlayer spacing, and ΔE_S is the amount of elastic strain energy released. We rewrite eq 1 as

$$\bar{E}_{\text{crack}} \times 6L + \Delta\bar{E}_{\text{interlayer}} \times 2.6L^2 = \Delta\bar{E}_s \times 2.6L^2 \quad (2)$$

where $\bar{E}_{\text{crack}}$ is the crack formation energy per unit crack length, $\Delta\bar{E}_{\text{interlayer}}$ is the work done to increase the interlayer spacing per unit area, $\Delta\bar{E}_s$ is the change in strain energy per unit area, $6L$ is the perimeter of the hexagon, and $2.6L^2$ is the area of the hexagon.

We approximate $\Delta\bar{E}_{\text{interlayer}}$ by the change in the van der Waals interaction energy between the graphene oxide sheets, which can be estimated as

$$U_{\text{vdW}} = -\frac{A_{\text{Ham}}}{12\pi l^2} \quad (3)$$

where A_{Ham} is the Hamaker constant and has been computed[3] to be 2.37×10^{-21} J; l is the separation between the sheets. After crack formation, due to undulation, the separation between the top two sheets should be larger than the interlayer spacing of graphite (0.34 nm) but should be smaller than ~0.7 nm, the spacing between fully oxidized graphene oxide sheets of GO (0.7 nm) since only one side of the uppermost graphene sheet is oxidized. Assuming the interlayer separation increases from 0.34 to 0.52 nm (average of 0.34 and 0.7 nm) (Figure 4d), $\Delta\bar{E}_{\text{interlayer}}$ is calculated to be 3.11×10^{-4} J/m^2.

We approximate the buildup of strain energy in graphene oxide by the energy associated with bending a pristine graphene sheet into a nanotube.[37] We recognize that the exact structure of graphene oxide is not yet known.[33,41] Both hydroxyl and epoxy groups can cause undulation of the sheets and affect the strain energy.[30,33] Thus, we only aim for an order of magnitude estimation for $\Delta\bar{E}_s$. To bend a 1.2 nm by 8.5 nm graphene sheet into a 2.4 nm-diameter tube, 0.84 eV of energy is needed.[37] This energy is normalized to yield a bending energy per unit area of 1.28×10^{-2} J/m^2. To calculate the strain energy released, we subtract the interlayer attraction after crack formation from the bending energy and obtain a strain energy released per unit area of 1.26×10^{-2} J/m^2.

The crack formation energy per unit crack length depends on the energy of the bonds that are broken as well as the number of bonds broken per unit crack length. Based on the existing graphite oxide models,[33,41] four types of bonds are present in graphene oxide sheets: carbon–carbon double bond (C=C), carbon–oxygen (C–O), carbon–carbon single bond (C–C) in which a hydroxyl group is attached to one of the

TABLE 1. Energies of Bonds in Graphene Oxides[43]

ruptured bond	bond energy (kJ/mol)
C═C	640
C—O	330
C—C in HO—C—C and HO—C—C—OH	345

TABLE 2. Cell Sizes Calculated Based on the Type of Bonds Broken during Crack Formation

ruptured bond	calculated edge length (μm)	cell size (μm)
C═C	0.68	1.18
C—O	0.35	0.61
C—C in HO—C—C and HO—C—C—OH	0.37	0.64

carbon atoms (HO—C—C), and the C—C bond in which hydroxyls are attached to both of the carbon atoms (HO—C—C—OH).[33] While the bond energies of C═C and C—O have been reported as 640 and 330 kJ/mol, respectively,[43] the energy of the C—C bond in HO—C—C—OH and HO—C—C has not been calculated previously. We approximate the energy of both bonds by the bond energy for a C—C bond in which hydrogen atoms are attached to both carbon atoms and yield a value of 345 kJ/mol[43] (Table 1). The actual bond energy may be different due to the presence of hydroxyl groups. The number of bonds broken per unit crack length, 3.40×10^9 bonds/m is estimated by placing a hexagon of arbitrary edge length on a graphene lattice and dividing the number of bonds intersecting with the boundaries of the hexagon by its perimeter.

Detailed calculations of the energy balance are summarized in the Appendix. As tabulated in Table 2, depending on which bonds are broken, the cell size ranges from 1.18 μm, assuming only the C═C bonds are broken, to 0.61 μm, if only the C—O bonds are broken. Crack formation in the experiments likely involves rupturing of all four types of bonds.

While the range of cell size predicted by this model is significantly lower than the experimentally observed cell size of ~16 μm, our model provides a conceptual mechanism for the periodic cracking observed experimentally. We explain the discrepancy between the cell size predicted theoretically and that observed experimentally as follows. First, the calculated $\Delta\bar{E}_s$ is 2 orders of magnitude higher than the interlayer interaction energy. As the suppression of graphene oxide undulation requires $\Delta\bar{E}_s$ to be smaller than the interaction energy, we expect the actual $\Delta\bar{E}_s$ to be significantly lowered than the approximated value as a result of the hydroxyl and epoxy groups. Second, we approximate $\Delta\bar{E}_{interlayer}$ as the van der Waals interaction between graphene oxide sheets. A more accurate determination of $\Delta\bar{E}_{interlayer}$ would require the calculation of the interaction energy between a partially oxidized

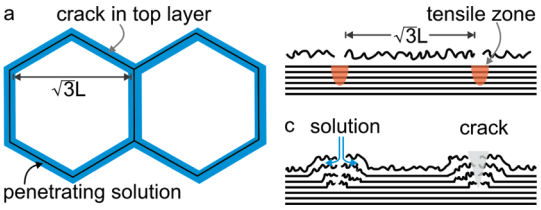

Figure 5. (a) Penetration of oxidizing solution underneath the uppermost graphene oxide layer. (b) Tensile zone formation upon periodic cracking of the uppermost graphene oxide layer. (c) Propagation of cracks in the cross-planar direction.

graphene sheet and a stack of pristine graphene sheets underneath it. Third, the actual bond energy of C—C in HO—C—C and HO—C—C—OH may be different than the approximated value, resulting in a different cell size. Finally, the model does not include the heat dissipation resulting from the lateral sliding associated with the undulation of graphene oxide sheets. Incorporation of the heat dissipation would result in a larger theoretical cell size and better agreement with experimental results.

To explain why the cell size is unchanged upon further oxidation, we note that upon periodic cracking, undulation of the graphene oxide sheets weakens the interlayer interaction energy. As a result, the sheets are allowed to further undulate as more hydroxyl and epoxy sites form. Strain energy is not built up and further crack formation is prevented.

Crack Propagation during the Cross-Planar Oxidation. We estimate an effective crack propagation rate based on the thickness of the GO layer observed in the optical microscopy images of HOPG oxidized for 6 s. Based on an average film thickness of 150 nm (assuming a refractive index of 1.5 for GO, Figure 3b), which corresponds to 214 layers of fully oxidized graphene oxide, a graphite layer of 72 nm is oxidized in 6 s and the crack propagation rate is calculated to be 12 nm/s.

To understand how cracking proceeds in graphene layers underneath the top sheet, we first estimate the average lateral penetration rate of the oxidizing solution between the graphene layers by examining the width of the GO films at the cell boundaries on HOPG oxidized for 6 s. The width ranges from 0.9 to 3.5 μm with an average value of 1.9 μm (Figure 2c). With this, we estimate an effective penetration rate of the oxidizing solution in the in-plane direction between graphene layers to be ~160 nm/s (0.95 μm/6 s). At this penetration rate, the oxidizing solution can only penetrate 950 nm along the second layer which is an order of magnitude less than what is needed to penetrate to the center of the cells (~8 μm) within 6 s (Figure 5a). Thus, unlike the first layer, the subsequent graphene layers crack before they are completely oxidized. We attribute this to stress concentration at the crack tips analogous to the mechanisms observed in brittle solids.[44,45] Here, the top layer's undulation to a fully

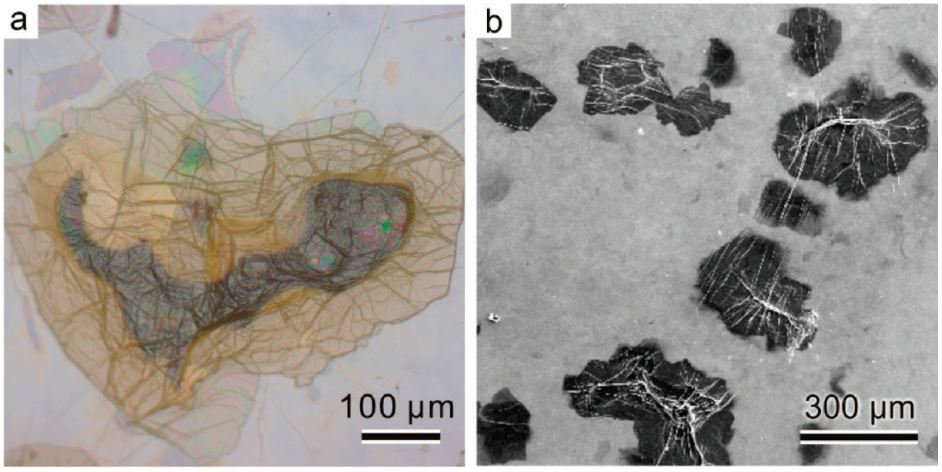

Figure 6. Optical microscopy (a) and SEM (b) image of graphite particles oxidized for 6 h.

relaxed state is constrained by its adhesive interaction with the layers underneath, thus leading to tensile zones at the crack tips (Figure 5b). As cracks propagate, followed by the lateral penetration of oxidizing solution between graphene layers, the interlayer separation increases, leading to the elevated cell edges (Figure 5c).

We also note that grain boundaries and ledges exist on the HOPG and oxidation can start preferentially at these sites.[46] However, the grain size of the HOPG is 3 mm (provided by the manufacturer), more than 2 orders of magnitude larger than the observed cell size. Further, the spacing between the ledges ranges from tens of nanometers[42] to a few micrometers,[46] significantly smaller than the ~16 μm cell size observed. Therefore, we conclude that crack formation at the grain boundaries and ledges cannot be the cause of the cellular structure.

Cross-planar and Edge-to-Center Oxidation of Graphite Particles. To contrast the effect of edge-to-center oxidation *versus* oxidation by cross-planar cracking, we examine graphite particles (~700 μm) oxidized for 6 h with optical microscopy. The image in Figure 6a reveals the presence of two regions in the particle. The edge of the particle has a brown-colored appearance which is likely the fully oxidized graphite region surrounding a zone of a partially oxidized and/or a nonoxidized region. Cracks and/or kinks[22] are observed as dark lines across the entire sample. Partial oxidation is further supported by the presence of a graphite peak as characterized by XRD (see SI1, Supporting Information). The SEM image of these partially oxidized GO particles, in Figure 6b, shows that the lateral dimensions of the GO particles range from 50 to 480 μm with a mean size at 170 μm. Upon complete oxidation for 12 h (SI1), the size of the GO particles is further reduced to 20−400 μm with a mean size at 120 μm, significantly larger than the cell size observed in cross-planar oxidation. We provide the following analysis to interpret this difference.

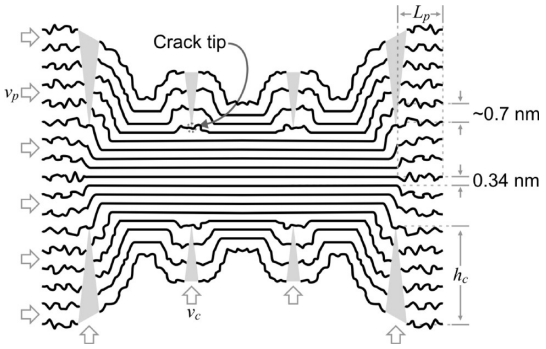

Figure 7. Schematics of crack propagation and penetration of oxidizing solution during the oxidation of a graphite particle immersed in an oxidizing solution.

During oxidation of graphite particles immersed in the oxidizing solution, crack propagation and edge-to-center penetration of oxidizing solution must take place simultaneously, as shown in Figure 7. The ratio of the effective solution penetration rate, $v_p = L_p/2t$, to the effective crack velocity, $v_c = h_c/2t$, where L_p is the penetration distance and h_c is the crack length for time t yields

$$\frac{L_p}{h_c} = \frac{v_p}{v_c} \quad (4)$$

Since $v_p/v_c \cong 10$, when the aspect ratio of the graphite particle, L/h is smaller than 10, we expect the core to be fully oxidized before the cracks reach the center thus yielding larger graphene oxide sheets. The adhesion between the cracked and the uncracked graphene oxide sheets holds them together and results in GO particles hundreds of micrometers in size, as shown in Figure 6. The presence of cracks on the surface of the GO particles likely contributes to the dark lines on the particles.

Size Reduction of Graphene Oxides by External Energy Input. The fluid motion generated by vigorous stirring can result in interparticle collisions as well as collisions between the particles and the wall of the beaker. These

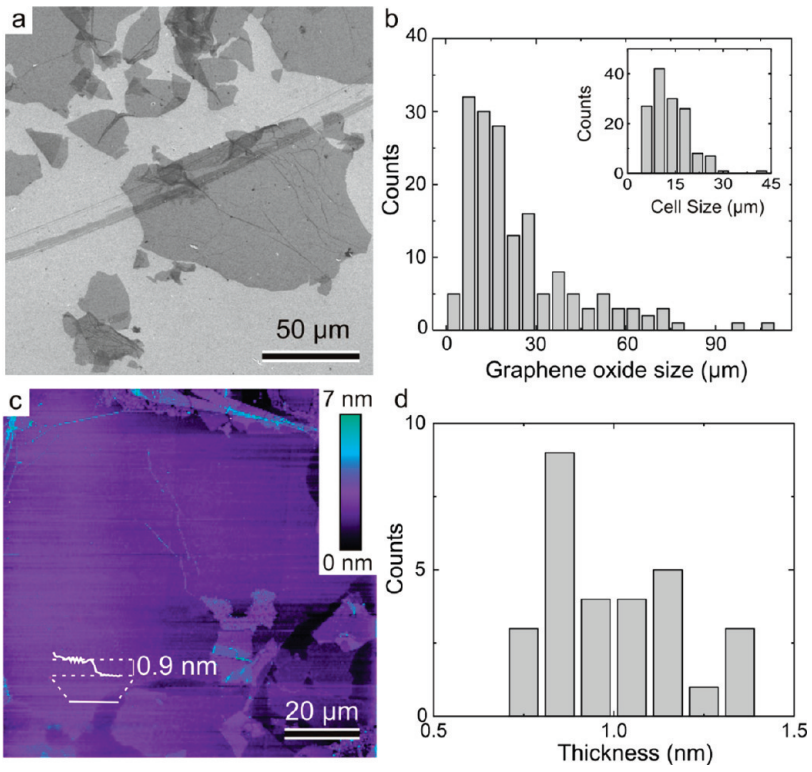

Figure 8. (a) SEM image of graphene oxide sheets obtained after 6 h of oxidation without mechanical shaking or sonication. (b) Histogram of the sizes of graphene oxide sheets; inset shows the histogram of cell sizes observed on an oxidized HOPG surface. (c) Tapping mode AFM image showing a single graphene oxide sheet that more than 100 μm in lateral size. (d) Histogram of the thicknesses of 30 sheets determined by AFM. A mean thickness of 0.93 nm is observed.

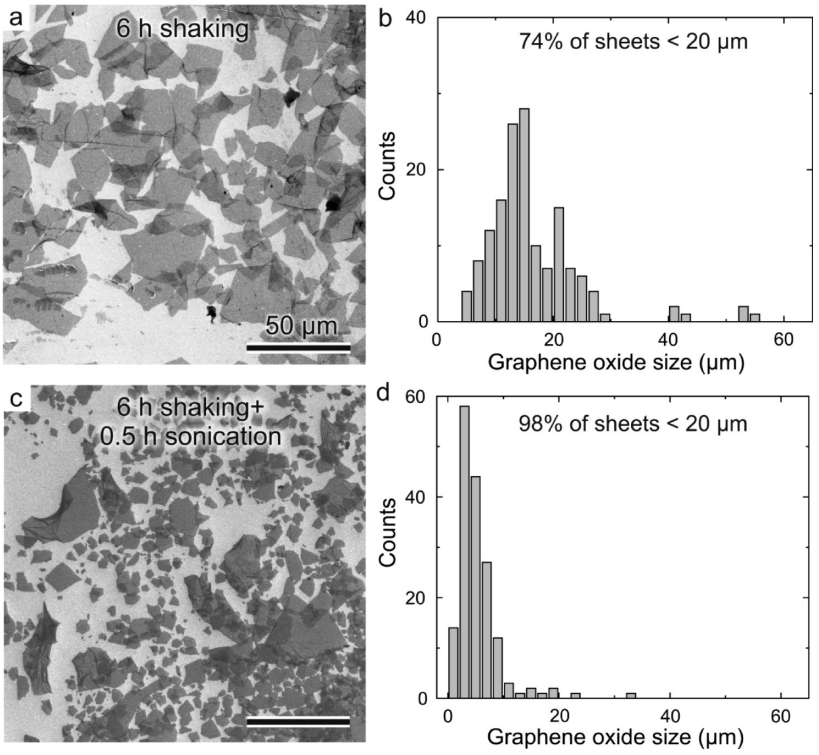

Figure 9. (a) SEM image of graphene oxide sheets that underwent 6 h of mechanical shaking. (b) Histogram of sheet sizes observed in panel a. (c) SEM image of graphene oxide sheets that underwent 6 h of mechanical shaking and 0.5 h of sonication. (d) histogram of sheet sizes observed in panel c. All the scale bars are 50 μm.

collisions can also cause a buildup of a tensile stress in the particles and thus crack formation. Another source of tensile stress is the drag force generated by the surrounding fluid flow.[47] It has been demonstrated that the magnitude of the drag force is proportional to the velocity of the fluid flow.[48]

To test the effect of external energy input, we first examined the graphene oxide sheets after the oxidation process where the energy input is limited to fluid motion caused by stirring during oxidation and washing. The lateral dimensions of the flakes determined from secondary electron SEM images (Figure 8a) range from 3 to over 100 μm (Figure 8b). However, we note that when the tail above 30 μm is left out, the size distribution is very similar to the distribution of cell sizes from a cross-planar oxidation of graphite (inset in Figure 8b) suggesting that this part of the distribution is produced through cross-planar cracking, whereas the larger ones are from the center zone. To test whether these flakes are individual graphene oxide sheets, we examined their thickness with tapping mode AFM. The sheet demonstrated in Figure 8c is over 100 μm in lateral dimensions and has a thickness of 0.9 nm. This thickness is very close to the single sheet thickness (0.71 nm) of graphene oxide determined by XRD,[3,22] confirming the presence of a single graphene oxide sheet. A mean thickness of 0.93 nm of 30 sheets (Figure 8d) is indicative of all single layer graphene oxide.

Additional mechanical energy input, such as mechanical shaking and sonication, further reduces the size of graphene oxide sheets (Figure 9). The percentage of sheets smaller than 20 μm increases from 58% without shaking to 74% with 6 h of shaking. With 6 h of shaking followed by 0.5 h of bath sonication, 98% of the sheets are now less than 10 μm. The size reduction of graphene oxide sheets obtained with shaking and sonication is more significant than that of the sheets obtained with 12 h of shaking alone (see SI2).

Graphene oxide sheets derived from fully oxidized graphite in the absence of long-duration shaking or sonication are limited to less than 10 μm in lateral dimension (see SI3), significantly smaller than those derived from partially oxidized graphite. We attribute this size reduction to the further weakening of graphene sheets resulting from the addition of hydroxyl and epoxy sites.

CONCLUSIONS

We have shown that the size of graphene oxide sheets derived from graphite oxide is affected by the path of oxidation and the input of mechanical energy. A cross-planar oxidation of graphite results in periodic cracking of the uppermost graphene oxide sheet, and subsequent crack propagation limits the size of the graphene oxide sheets to less than 30 μm. We explain the periodic cracking by the balance between the elastic strain energy buildup due to the undulation caused by the hydroxyl and epoxy sites, the crack formation energy, and the interaction energy between graphene layers. We also demonstrate that for graphite particles dispersed in an oxidizing solution, oxidation takes place through both cross-planar and edge-to-center paths and the aspect ratio of graphite particles determines the size of the resulting graphene oxide sheets. When the core of a graphite particle is fully oxidized by edge-to-center penetrating solution before the cracks reach the middle of the particle, large graphene oxide sheets (>100 μm) are produced. External mechanical energy input, in the form of shaking and sonication, creates fluid motion and that results in the buildup of a tensile load in the sheets and thus their size reduction.

MATERIALS AND METHODS

Materials. HOPG with a grain size up to 3 mm (Grade SPI-1) was purchased from SPI Supplies (West Chester, PA). Natural graphite particles, sized at ~700 μm (Grade 3061) were kindly provided by Asbury Carbons (Asbury, NJ). Potassium permanganate (Acros, 99+%), potassium nitrate (EM Science, 98%), sodium nitrate (EM Science, 98%), sulfuric acid (Spectrum Chemical, 98%), and hydrogen peroxide-water solution (Aldrich, 30−32 wt % in water) were used for the oxidation of HOPG surfaces and graphite particles according to the Hummers method.[20]

Oxidation of HOPG Surfaces. An HOPG film was cleaved from a block of HOPG with an adhesive paper tape and anchored onto a polystyrene Petri-dish. A sessile drop of an oxidizing solution (55 mL of sulfuric acid, 6.3 g of sodium nitrate, and 1 g of potassium permanganate) was deployed onto the HOPG surfaces. The reaction was allowed to proceed for 6 s, 60 s, and 10 min. The oxidized surfaces were rinsed with deionized water purified with Picopure 2 water purification system (Hydro Service and Supplies Inc., Durham, NC) and blow-dried with dry nitrogen for 2 min.

Oxidation of Graphite Particles. Potassium nitrate (1.1 g) was first dissolved in 40 mL of sulfuric acid under stirring with a magnetic stir bar. Graphite particles (0.9 g) were added to the acid solution and the mixture was stirred for 5 min, followed by the addition of potassium permanganate (5.2 g). The oxidation was allowed to proceed for 6 and 12 h. On completion of the reaction, 20 mL of the suspension was extracted and added to 120 mL of deionized water, followed by the addition of hydrogen peroxide-water solution (2.6 mL). The GO particles were washed repeatedly with deionized water until the pH of the suspension was neutral. Finally, the suspension was diluted with deionized water to a total volume of 200 mL in a 500 mL flask.

Preparation of Langmuir−Blodgett (LB) Films of Graphene Oxide from GO. Three different GO−water suspensions were used to prepare LB films: (i) an as-produced suspension; (ii) a suspension that underwent mechanical shaking (model 75, Burrell Scientific, Pittsburgh, PA) for 6 h; (iii) 40 mL of suspension that was bath-sonicated for 0.5 h (model 2510, Branson Ultrasonics, Danbury, CT).

All three suspensions were centrifuged for 10 min at 2000 rpm to remove unexfoliated GO particles. The supernatant (1 mL) was extracted and diluted with 5 mL of methanol (EMD Chemicals, 99.8%). The diluted suspension was added dropwise into an LB trough (NIMA Technology, Linthicum Heights, MD)

using a glass syringe. Surface pressure was monitored using a tensiometer attached to a Wilhelmy plate. The graphene oxide film was compressed by barriers at a speed of 30 mm/min until the surface pressure reached 3 mN/m. The film was then transferred onto a vertical gold-coated silicon or mica substrate using a dip-coating device (NIMA Technology) at a withdrawing speed of 1 mm/min and dried at room temperature.

AFM Characterization. Oxidized HOPG surfaces were examined by AFM (MultiMode Nanoscope IIIa, Veeco Metrology, Santa Barbara, CA) in contact-mode with a Veeco NP-S silicon nitride tip (spring constant k = 0.32 N/m, and radius of curvature r = 20 nm). Graphene oxide sheets deposited on a mica substrate were examined in tapping-mode with a Veeco RTESP silicon tip (k = 20−80 N/m, r = 10 nm, and resonance frequency f = 270−312 kHz).

Optical Microscopy Characterization. Oxidized HOPG surfaces were examined by bright-field (BF) optical microscopy (Zeiss Axioplan 2, Carl Zeiss MicroImaging Inc., Thornwood, NY). Samples of GO were prepared by placing a droplet of GO suspension shaken for 6 h onto a glass slide and dried at room temperature prior to the optical microscopy characterization. Images were recorded using a 12-bit digital CCD camera (AxioCam HRc, Carl Zeiss MicroImaging Inc.), and stored in a computer for further analysis.

SEM Characterization. SEM samples of GO were prepared by placing a droplet of dilute GO−water suspension (0.1 g/mL) onto a silicon wafer and allowing the water to evaporate. The GO and graphene oxide particles were then examined by SEM (5130MM, Tescan USA Inc., Cranberry Twp., PA) in the secondary electron mode at an acceleration voltage of 5 kV.

APPENDIX

Detailed Calculation of the Energy Balance. The calculated values of $\Delta\bar{E}_S$ and $\Delta\bar{E}_{interlayer}$ are 1.26×10^{-2} and 3.11×10^{-4} J/m^2, respectively. $\bar{E}_{crack}$ is the product of the bond energy and the average number of bonds ruptured per unit crack length (3.40×10^9 bonds/m). Inputting these values into the eq 2 yields

$$3.40 \times 10^9 \times 6L \times \text{bond energy} + 3.11 \times 10^{-4} \times 2.6L^2 = 1.26 \times 10^{-2} \times 2.6L^2 \quad \textbf{(A1)}$$

where L is in the unit of meter and bond energy is in the unit of joule. L is then given by

$$L = 6.38 \times 10^{11}\ (\text{m/J}) \times \text{bond energy (J)} \quad \textbf{(A2)}$$

We then incorporate the different bond energies and calculate L.

Acknowledgment. This work was supported by the Army Research Office Multidisciplinary University Research Institute (ARO/MURI) under Grant No. W911NF-09-1-0476, the National Science Foundation NIRT under Grant No. CMS-0609049, and the NASA University Research, Engineering, and Technology Institute on BioInspired Materials (BIMat) under Award No. NCC-1-02037. We thank C. Punckt for assistance in the analysis of the optical microscopy images and R. K. Prud'homme for helpful comments.

Supporting Information Available: XRD patterns of graphite and GO; effect of 12-h mechanical shaking on the size of graphene oxide; effect of full oxidation on the size of graphene oxide. This material is available free of charge *via* the Internet at http://pubs.acs.org.

REFERENCES AND NOTES

1. Lee, C.; Wei, X. D.; Kysar, J. W.; Hone, J. Measurement of the Elastic Properties and Intrinsic Strength of Monolayer Graphene. *Science* **2008,** *321*, 385–388.
2. Bolotin, K. I.; Sikes, K. J.; Jiang, Z.; Klima, M.; Fudenberg, G.; Hone, J.; Kim, P.; Stormer, H. L. Ultrahigh Electron Mobility in Suspended Graphene. *Solid State Commun.* **2008,** *146*, 351–355.
3. McAllister, M. J.; Li, J. L.; Adamson, D. H.; Schniepp, H. C.; Abdala, A. A.; Liu, J.; Herrera-Alonso, M.; Milius, D. L.; Car, R.; Prud'homme, R. K.; *et al.* Single Sheet Functionalized Graphene by Oxidation and Thermal Expansion of Graphite. *Chem. Mater.* **2007,** *19*, 4396–4404.
4. Wang, D. H.; Choi, D. W.; Li, J.; Yang, Z. G.; Nie, Z. M.; Kou, R.; Hu, D. H.; Wang, C. M.; Saraf, L. V.; Zhang, J. G.; *et al.* Self-Assembled TiO_2−Graphene Hybrid Nanostructures for Enhanced Li-Ion Insertion. *ACS Nano* **2009,** *3*, 907–914.
5. Wang, D. H.; Kou, R.; Choi, D.; Yang, Z. G.; Nie, Z. M.; Li, J.; Saraf, L. V.; Hu, D. H.; Zhang, J. G.; Graff, G. L.; *et al.* Ternary Self-Assembly of Ordered Metal Oxide−Graphene Nanocomposites for Electrochemical Energy Storage. *ACS Nano* **2010,** *4*, 1587–1595.
6. Kim, H.; Miura, Y.; Macosko, C. W. Graphene/Polyurethane Nanocomposites for Improved Gas Barrier and Electrical Conductivity. *Chem. Mater.* **2010,** *22*, 3441–3450.
7. Ramanathan, T.; Abdala, A. A.; Stankovich, S.; Dikin, D. A.; Herrera-Alonso, M.; Piner, R. D.; Adamson, D. H.; Schniepp, H. C.; Chen, X.; Ruoff, R. S.; *et al.* Functionalized Graphene Sheets for Polymer Nanocomposites. *Nat. Nanotechnol.* **2008,** *3*, 327–331.
8. Kim, H.; Macosko, C. W. Morphology and Properties of Polyester/Exfoliated Graphite Nanocomposites. *Macromolecules* **2008,** *41*, 3317–3327.
9. Kim, H.; Macosko, C. W. Processing-Property Relationships of Polycarbonate/Graphene Composites. *Polymer* **2009,** *50*, 3797–3809.
10. Stankovich, S.; Dikin, D. A.; Dommett, G. H. B.; Kohlhaas, K. M.; Zimney, E. J.; Stach, E. A.; Piner, R. D.; Nguyen, S. T.; Ruoff, R. S. Graphene-Based Composite Materials. *Nature* **2006,** *442*, 282–286.
11. Kou, R.; Shao, Y. Y.; Wang, D. H.; Engelhard, M. H.; Kwak, J. H.; Wang, J.; Viswanathan, V. V.; Wang, C. M.; Lin, Y. H.; Wang, Y.; *et al.* Enhanced Activity and Stability of Pt Catalysts on Functionalized Graphene Sheets for Electrocatalytic Oxygen Reduction. *Electrochem. Commun.* **2009,** *11*, 954–957.
12. Wu, H.; Wang, J.; Kang, X. H.; Wang, C. M.; Wang, D. H.; Liu, J.; Aksay, I. A.; Lin, Y. H. Glucose Biosensor Based on Immobilization of Glucose Oxidase in Platinum Nanoparticles/Graphene/Chitosan Nanocomposite Film. *Talanta* **2009,** *80*, 403–406.
13. Sabourin, J. L.; Dabbs, D. M.; Yetter, R. A.; Dryer, F. L.; Aksay, I. A. Functionalized Graphene Sheet Colloids for Enhanced Fuel/Propellant Combustion. *ACS Nano* **2009,** *3*, 3945–3954.
14. Stoller, M. D.; Park, S. J.; Zhu, Y. W.; An, J. H.; Ruoff, R. S. Graphene-Based Ultracapacitors. *Nano Lett.* **2008,** *8*, 3498–3502.
15. Li, X. S.; Cai, W. W.; An, J. H.; Kim, S.; Nah, J.; Yang, D. X.; Piner, R.; Velamakanni, A.; Jung, I.; Tutuc, E.; *et al.* Large-Area Synthesis of High-Quality and Uniform Graphene Films on Copper Foils. *Science* **2009,** *324*, 1312–1314.
16. Reina, A.; Jia, X. T.; Ho, J.; Nezich, D.; Son, H. B.; Bulovic, V.; Dresselhaus, M. S.; Kong, J. Large Area, Few-Layer Graphene Films on Arbitrary Substrates by Chemical Vapor Deposition. *Nano Lett.* **2009,** *9*, 30–35.
17. Kim, K. S.; Zhao, Y.; Jang, H.; Lee, S. Y.; Kim, J. M.; Ahn, J. H.; Kim, P.; Choi, J. Y.; Hong, B. H. Large-Scale Pattern Growth of Graphene Films for Stretchable Transparent Electrodes. *Nature* **2009,** *457*, 706–710.
18. Sutter, P. W.; Flege, J. I.; Sutter, E. A. Epitaxial Graphene on Ruthenium. *Nat. Mater.* **2008,** *7*, 406–411.
19. Novoselov, K. S.; Geim, A. K.; Morozov, S. V.; Jiang, D.; Zhang, Y.; Dubonos, S. V.; Grigorieva, I. V.; Firsov, A. A. Electric Field Effect in Atomically Thin Carbon Films. *Science* **2004,** *306*, 666–669.
20. Hummers, W. S.; Offeman, R. E. Preparation of Graphite Oxide. *J. Am. Chem. Soc.* **1958,** *80*, 1339–1339.
21. Staudenmaier, L. *Ber. Dtsch. Chem. Ges.* **1898,** *31*, 1481.
22. Schniepp, H. C.; Li, J. L.; McAllister, M. J.; Sai, H.; Herrera-Alonso, M.; Adamson, D. H.; Prud'homme, R. K.; Car, R.; Saville, D. A.; Aksay, I. A. Functionalized Single Graphene

Sheets Derived from Splitting Graphite Oxide. *J. Phys. Chem. B* **2006,** *110*, 8535–8539.
23. Hicks, J.; Behnam, A.; Ural, A. A Computational Study of Tunneling-Percolation Electrical Transport in Graphene-Based Nanocomposites. *Appl. Phys. Lett.* **2009,** *95*, 213103.
24. Kelly, A.; Tyson, W. R. Tensile Properties of Fibre-Reinforced Metals—Copper/Tungsten and Copper/Molybdenum. *J. Mech. Phys. Solids* **1965,** *13*, 329–350.
25. Nielsen, L. E. Models for the Permeability of Filled Polymer Systems. *J. Macromol. Sci. A* **1967,** *A1*, 929–942.
26. Li, C. Y.; Thostenson, E. T.; Chou, T. W. Dominant Role of Tunneling Resistance in the Electrical Conductivity of Carbon Nanotube-Based Composites. *Appl. Phys. Lett.* **2007,** *91*, 223114.
27. Zhao, J. P., S.; Ren, W.; Gao, L.; Cheng, H. Efficient Preparation of Large-Area Graphene Oxide Sheets for Transparent Conductive Films. *ACS Nano* **2010,** *4*, 5245–5252.
28. Zhang, L.; Liang, J. J.; Huang, Y.; Ma, Y. F.; Wang, Y.; Chen, Y. S. Size-Controlled Synthesis of Graphene Oxide Sheets on a Large Scale Using Chemical Exfoliation. *Carbon* **2009,** *47*, 3365–3368.
29. Su, C. Y.; Xu, Y. P.; Zhang, W. J.; Zhao, J. W.; Tang, X. H.; Tsai, C. H.; Li, L. J. Electrical and Spectroscopic Characterizations of Ultralarge Reduced Graphene Oxide Monolayers. *Chem. Mater.* **2009,** *21*, 5674–5680.
30. Li, J. L.; Kudin, K. N.; McAllister, M. J.; Prud'homme, R. K.; Aksay, I. A.; Car, R. Oxygen-Driven Unzipping of Graphitic Materials. *Phys. Rev. Lett.* **2006,** *96*, 176101.
31. Tung, V. C.; Allen, M. J.; Yang, Y.; Kaner, R. B. High-Throughput Solution Processing of Large-Scale Graphene. *Nat. Nanotechnol.* **2009,** *4*, 25–29.
32. Zhou, X. F.; Liu, Z. P. A Scalable, Solution-Phase Processing Route to Graphene Oxide and Graphene Ultralarge Sheets. *Chem. Commun.* **2010,** *46*, 2611–2613.
33. Kudin, K. N.; Ozbas, B.; Schniepp, H. C.; Prud'homme, R. K.; Aksay, I. A.; Car, R. Raman Spectra of Graphite Oxide and Functionalized Graphene Sheets. *Nano Lett.* **2008,** *8*, 36–41.
34. Chow, T. S.; Liu, C. A.; Penwell, R. C. Direct Determination of Interfacial Energy Between Brittle and Polymeric Films. *J. Polym. Sci., Polym. Phys.* **1976,** *14*, 1305–1310.
35. Davutoglu, A.; Aksay, I. A. The Work of Adhesion Measurements by a Periodic Cracking Technique. In *Surfaces and Interfaces in Ceramic and Ceramic-Metal Systems*; Pask, J. A., Evans, A. G., Eds.; Plenum: New York, 1981; pp 641–649.
36. Schulze, G. W.; Erdogan, F. Periodic Cracking of Elastic Coatings. *Int. J. Solids Struct.* **1998,** *35*, 3615–3634.
37. Schniepp, H. C.; Kudin, K. N.; Li, J. L.; Prud'homme, R. K.; Car, R.; Saville, D. A.; Aksay, I. A. Bending Properties of Single Functionalized Graphene Sheets Probed by Atomic Force Microscopy. *ACS Nano* **2008,** *2*, 2577–2584.
38. Born, M.; Wolf, W. *Principles of Optics*; Cambridge University Press: Cambridge, 2002.
39. Ergun, S.; Yasinsky, J. B.; Townsend, J. R. Transverse and Longitudinal Optical Properties of Graphite. *Carbon* **1967,** *5*, 403–408.
40. Jeong, H. K.; Jin, M. H.; An, K. H.; Lee, Y. H. Structural Stability and Variable Dielectric Constant in Poly Sodium 4-Styrensulfonate Intercalated Graphite Oxide. *J. Phys. Chem. C* **2009,** *113*, 13060–13064.
41. Lerf, A.; He, H. Y.; Forster, M.; Klinowski, J. Structure of Graphite Oxide Revisited. *J. Phys. Chem. B* **1998,** *102*, 4477–4482.
42. Schniepp, H. C.; Shum, H. C.; Saville, D. A.; Aksay, I. A. Orientational Order of Molecular Assemblies on Rough Surfaces. *J. Phys. Chem. C* **2008,** *112*, 14902–14906.
43. Oxtoby, D. W.; Gillis, H. P.; Nachtrieb, N. H. *Principles of Modern Chemistry*, 5th ed.; Thomson Brooks/Cole: New York, 2002.
44. Griffith, A. A. The Phenomena of Rupture and Flow in Solids. *Philos. Trans. R. Soc. A* **1921,** *221*, 163–198.
45. Xu, S. W.; Deng, X. M. Nanoscale Void Nucleation and Growth and Crack Tip Stress Evolution Ahead of a Growing Crack in a Single Crystal. *Nanotechnology* **2008,** *19*, 15.
46. Paredes, J. I.; Martinez-Alonso, A.; Tascon, J. M. D. Multiscale Imaging and Tip-Scratch Studies Reveal Insight into the Plasma Oxidation of Graphite. *Langmuir* **2007,** *23*, 8932–8943.
47. Hennrich, F.; Krupke, R.; Arnold, K.; Stutz, J. A. R.; Lebedkin, S.; Koch, T.; Schimmel, T.; Kappes, M. M. The Mechanism of Cavitation-Induced Scission of Single-Walled Carbon Nanotubes. *J. Phys. Chem. B* **2007,** *111*, 1932–1937.
48. Keller, J. B.; Rubinow, S. I. Slender-Body Theory for Slow Viscous-Flow. *J. Fluid Mech.* **1976,** *75*, 705–714.